Journal of Sound and Vibration 536 (2022) 117098

Contents lists available at ScienceDirect

Journal of Sound and Vibration

journal homepage: www.elsevier.com/locate/jsvi

Baseline-free structural damage identification for plate-like structures based on two-dimensional curvature propagating flexural waves

Wei Zhou, Y.F. Xu *, J.S. Kim

Department of Mechanical and Materials Engineering, University of Cincinnati, Cincinnati, OH 45221, USA

ARTICLE INFO

Keywords:
Baseline-free structural damage identification
Teager energy operator
Two-dimensional curvature propagating flexural waves
Two-dimensional continuous wavelet transform

ABSTRACT

Waveforms of propagating flexural waves can reveal plentiful information about local anomalies caused by damage, and the local anomalies can be used for damage identification. However, the local anomalies can be masked by the interference of measurement noise and global trends of the waveforms, and they may be able to indicate only fractions of the size and extent of the damage. In this paper, an effective noise-robust damage identification method for plate-like structures is proposed based on the fact that damage can introduce imminent local anomalies to two-dimensional curvature propagating flexural waves (2D-CPFW). The 2D-CPFW can be alternated using two-dimensional continuous wavelet transform (2D-CWT) to lower adverse effects of measurement noise and errors. To suppress global trends and intensify the local anomalies in the 2D-CPFW, 2D-CWT with a higher-order Laplacian of Gaussian function and the Teager energy operator are applied. The fundamental mechanism of how 2D-CWT with different orders of Laplacians of Gaussian function can suppress global trends of 2D-CPFW is investigated for the first time. It is found that the rth-order Laplacian of Gaussian function can well suppress the global trend of a 2D-CPFW within a finite interval if the trend can be well approximated by a $(2r-1)$th-order bi-variant polynomial. The modal assurance criterion and a statistical criterion are used to assist the selection of the proper order of Laplacian of Gaussian function. An accumulative damage index is proposed, and the locations and extent of the damage can be identified within neighborhoods with high damage index values. If an intact plate-like structure is geometrically smooth and made of materials that have no mass and stiffness discontinuities, the proposed method does not require any waveforms of the intact structure serving as a baseline, and therefore, the method can be considered baseline-free. Effectiveness and noise-robustness of the proposed method are investigated in two numerical examples. Two experimental investigations were conducted on two aluminum plates under different damage scenarios. Both the numerical and experimental examples verify that the proposed method is effective and noise-robust in identifying the location and extent of the damage.

1. Introduction

Structures in service for mechanical, aerospace, and civil engineering purposes can suffer from aging and deterioration due to everlasting environmental effects and operational loads. To avoid catastrophic structural failures, structural health monitoring is

* Corresponding author.
E-mail addresses: zhouw6@mail.uc.edu (W. Zhou), xu2yf@uc.edu (Y.F. Xu), kim5jk@mail.uc.edu (J.S. Kim).

https://doi.org/10.1016/j.jsv.2022.117098
Received 24 September 2021; Received in revised form 20 May 2022; Accepted 3 June 2022
Available online 11 June 2022
0022-460X/

critical by identifying existing developing deterioration and assessing their conditions [1–3]. Vibration-based damage identification has been a main research topic of structural dynamics applications in recent decades. Quantitative changes in local stiffness and/or mass can occur when local damage exists in a structure [4–7]. Hence, vibration characteristics of the structure, such as natural frequencies, operating deflection shapes, and mode shapes, can be used for damage identification. The natural frequencies-based methods are generally used for global identification, as they can be estimated with excitation and response points that are away from the damage [8]. Adams et al. [9] found that a damage state of a structure can be identified as reduction in stiffness, which leads to changes of its natural frequencies. A damage identification technique based on changes of natural frequencies was investigated by comparing natural frequencies at pristine and damage states [10]. The mode shapes and operating deflection shapes based methods are considered local identification, as local anomalies cannot be identified if the locality of the anomalies falls beyond a measurement grid [8]. Besides, mode shapes and operating deflection shapes-based methods are vulnerable to measurement noise and only relatively large damage is identifiable by using local anomalies in mode shapes and operating deflection shapes [11]. The use of curvatures of mode shapes and operating deflection shapes, referred to as curvature mode shapes and curvature operating deflection shapes, respectively, for damage identification were proposed in Refs. [12] and [13], respectively. It was shown that curvature mode shapes and curvature operating deflection shapes are more sensitive to small damage than mode shapes and operating deflection shapes. One the other hand, uses of continuous wavelet transforms (CWTs) were proposed and investigated in Refs. [14–17] to accurately calculate the curvature mode shapes. The multi-scale property of CWT can reduce adverse effects of measurement noise and the effects can be further reduced by adjusting the value of its scale parameter. However, global trends in curvature mode shapes and curvature operating deflection shapes can mask their local anomalies caused by damage and prevent accurate identification results. To address this problem, Teager energy operator (TEO) has been applied to further intensify local anomalies for damage identification based on CWT curvature mode shapes [18,19]. TEO can intensify local anomalies and minimize fluctuation of global trends. Its use was introduced by combining CWT for identification of multiple damage for beams in Ref. [18]. Two-dimensional (2D) TEO was applied to intensify local anomalies of 2D-CWT curvature mode shapes for plates-like structures [19].

As a type of elastic waves propagating in a thin plate/shell structure, Lamb waves were first described and studied by Sir Horace Lamb [20]. Dispersion relations exist in Lamb waves, which can be observed in dispersion curves: velocities of Lamb wave propagation, including phase and group velocities, depend on the frequency-thickness product, and the curves are determined by the mass density and Young's modulus of the structure. Based on dispersion curves, one finds that at a certain frequency-thickness product, symmetric and antisymmetric Lamb wave modes simultaneously exist. The nth symmetric and antisymmetric Lamb wave modes are usually denoted by Sn and An modes, respectively. Lamb waves can propagate for long distances in plate/shell structures so that plentiful information of local anomalies caused by damage-wave interactions can be captured and manifested by appropriate post-processing. Lamb waves-based methods have been investigated and applied for damage identification in recent decades. The use of Lamb waves measured by a scanning laser Doppler vibrometers (SLDV) constitutes one type of the Lamb waves-based methods, which was first introduced in Ref. [21] and maximum amplitudes of Lamb waves were studied for damage identification in Ref. [22]. For further exploitation, root mean square (RMS) values of all waveforms of Lamb waves were used to formulate a damage index in Ref. [23]. An integral mean value damage index was introduced in Ref. [24] and compared with the damage index based on RMS values. It was shown that the damage index based on RMS values is more sensitive to the existence of damage and less sensitive to that of environmental noise. Ruzzene [25] introduced the frequency–wavenumber domain analysis for damage identification by using waveforms obtained by a SLDV. The analysis is capable of eliminating incident waves and separating wave modes to highlight the presence of reflected waves associated with damage. Yu et al. [26] introduced a short-space 2D Fourier transform to process Lamb waves. It yielded a frequency–wavenumber spectra at various spatial locations for damage identification. Recently, damage identification methods based on curvatures of waveforms of Lamb waves were studies in Refs. [8,27]. A theoretical basis of the methods is that curvature mode shapes have proved more damage-sensitive than mode shapes and used for damage identification. Sha et al. [27] introduced a concept of wavefield curvatures by calculating curvatures of waveforms of Lamb waves at selected time instants, and an energy image was then formed as square sums of the curvatures. Xu et al. [8] presented curvature of waveforms of propagating flexural waves by using local-regression polynomials to estimate curvature waveforms of a pseudo-pristine structure, which serve as baseline information for damage identification.

In this work, a baseline-free structural damage identification method is proposed for plate-like structures. It identifies location and extent of damage based on 2D curvature propagating flexural waves (2D-CPFWs), which are analogous to 2D curvature mode shapes in Ref. [19]. A 2D-CWT of propagating flexural waves (PFWs) with the Laplacian of Gaussian function, namely CWT-PFWs, is used to alternate 2D-CPFWs for alleviating interference of measurement noise. A two-phase local anomalies intensification method is proposed: (1) 2D-CWT of 2D-CPFWs with higher-order Laplacian of Gaussian function (CWT-CPFWs) be calculated to suppress the global trends of 2D-CPFWs and (2) TEO be applied to further suppress the trends and intensify the local anomalies. The mechanism of the 2D-CWT suppressing the global trends of 2D-CPFWs is investigated and explained, and the modal assurance criterion and a statistical criterion are used to determine the proper order of Laplacian of Gaussian function in the 2D-CWT. An accumulative damage index is proposed to obtain a complete identification of the damage based on Teager energy of CWT-CPFWs. A convergence index is introduced to determine which waveforms are included. Numerical investigations are conducted to study the effectiveness and noise-robustness of the proposed method for calculating the accumulative damage index. Experimental investigations were also conducted on damaged aluminum plates to validate the effectiveness of the proposed method.

The rest of the paper is arranged as follows. In Section 2, the proposed damage identification method based on 2D-CPFWs is presented. In Sections 3 and 4, the numerical and experimental investigations are presented, respectively. Concluding remarks of this work are presented in Section 5.

2. Methodology

2.1. Formulation of 2D-CPFWs for plate-like structures

According to typical phase velocity dispersion curves of a plate-like structure, at an adequately low frequency-thickness product, only S0 and A0 modes exist in its Lamb waves [28]. Further, it has been shown that cross-section flexural deformations of A0 Lamb wave modes are similar to those of PFWs [28] and the A0 Lamb wave modes are dominant over the S0 Lamb wave modes at adequately low frequency-thickness products [21,29]. Hence Lamb waves at adequately low frequency-thickness products can be well approximated by PFWs. A PFW of a plate-like structure can be considered as a three-dimensional spatial–temporal signal, as it consists of 2D waveforms at different time instants denoted by t. A waveform of the PFW at t, denoted by $W_t(x,y)$, can be considered as an instantaneous deformation with x and y being the spatial coordinates of a point on the structure. The 2D-CPFW refers to mean curvature of W_t and it can be expressed by [30]

$$\kappa_t = \kappa_{x,t} + \kappa_{y,t} = \Delta W_t(x,y) \tag{1}$$

where

$$\begin{cases} \kappa_{x,t} = \frac{\partial^2 W_t(x,y)}{\partial x^2} \\ \kappa_{y,t} = \frac{\partial^2 W_t(x,y)}{\partial y^2} \end{cases} \tag{2}$$

denote curvature PFWs along x- and y-axes, respectively, and Δ is the Laplace operator. The instantaneous bending moments of the structure at a spatial point along x- and y-axes, denoted by $M_{x,t}$ and $M_{y,t}$, respectively, can be calculated by

$$M_{x,t}(x,y) = -D(x,y)\left(\kappa_{x,t} + \nu\kappa_{y,t}\right) \tag{3}$$

and

$$M_{y,t}(x,y) = -D(x,y)\left(\kappa_{y,t} + \nu\kappa_{x,t}\right) \tag{4}$$

respectively, where

$$D(x,y) = \frac{Eh^3}{12\left(1-\nu^2\right)} \tag{5}$$

is the flexural rigidity of the structure at (x,y), in which E and ν denote the Young's modulus and Poisson's ratio, respectively, and h denotes the thickness of the structure. Summing up Eqs. (3) and (4) yields

$$M_{x,t}(x,y) + M_{y,t}(x,y) = -D(x,y)(1+\nu)\left(\kappa_{x,t} + \kappa_{y,t}\right) \tag{6}$$

Rearranging Eq. (6) and applying Eq. (1) yield

$$\kappa_t = -\frac{M_{x,t}(x,y) + M_{y,t}(x,y)}{D(x,y)(1+\nu)} \tag{7}$$

When small-size damage occurs to the structure, the value of D will change within the neighborhood of the damage, and more importantly, local anomalies occur to κ_t and 2D-CPFW as well. The local anomalies in the 2D-CPFW can be used to reveal the existence of the damage.

A 2D-CPFW can be obtained using the second-order central finite difference scheme [30]. However, the scheme may drastically amplify adverse effects of measurement noise and errors in PFW [19]. It is proposed that 2D-CWT of PFWs with the Laplacian of Gaussian function (CWT-PFWs) be calculated as an alternative of 2D-CPFWs [19]. Gaussian function can be expressed by

$$g(x,y) = \frac{1}{\sqrt{\pi}} e^{-\left(x^2+y^2\right)} \tag{8}$$

and a translatable and scalable family of Gaussian functions can be expressed by

$$g_{u,v,s}(x,y) = \frac{1}{s} g\left(\frac{x-u}{s}, \frac{y-v}{s}\right) \tag{9}$$

where s is the scale parameter, and u and v are translation parameters along x- and y-axes, respectively. The alternative of 2D-CPFW, referred to as CWT-PFW, can be expressed by [31]

$$\widehat{W}_t(u,v,s) = \int_{-\infty}^{\infty}\int_{-\infty}^{\infty} W_t(x,y)\,\Delta g_{u,v,s}(x,y)\,\mathrm{d}x\mathrm{d}y = \left(\Delta\tilde{g}_s \otimes W_t\right)(u,v) \tag{10}$$

where

$$\Delta\tilde{g}_s(x,y) = s^2\left(\frac{\partial^2}{\partial x^2} + \frac{\partial^2}{\partial y^2}\right)\tilde{g}_s(x,y) = \frac{1}{s}\Delta g\left(\frac{-x}{s}, \frac{-y}{s}\right) \tag{11}$$

and $\otimes$ denotes convolution. More details of the 2D-CWT can be found in Appendix. Based on the differentiation property of convolution [32], one has

$$\widehat{W}_t(u,v,s) = \left(\Delta\tilde{g}_s \otimes W_t\right)(u,v) = \left(s^2\tilde{g}_s \otimes \Delta W_t\right)(u,v) = \Delta\left(s^2\tilde{g}_s \otimes W_t\right)(u,v) \tag{12}$$

It is indicated by Eq. (12) that the calculation of CWT-PFW is equivalent to application of Δ to $s^2\tilde{g}_s \otimes W_t$. The term $s^2\tilde{g}_s \otimes W_t$ indicates that the adverse effects of the measurement noise and errors in W_t can be alleviated by the convolution of $s^2\tilde{g}_s$ with $\tilde{g}_s$ that acts as a low-pass filter. The application of Δ to the $s^2\tilde{g}_s \otimes W_t$ for CWT-PFW will not suffer from the amplified adverse effects of the measurement noise and errors, compared with those from a finite difference scheme for 2D-CPFW.

2.2. Local anomalies intensification

Though local anomalies caused by damage in PFWs can be identified in CWT-PFWs, they can be masked by global trends of CWT-PFWs, similar to those in curvature mode shapes [18,33], where TEO was applied to suppress the global trends and intensify damage-caused local anomalies [18,34]. However, it is observed in this work that the direct application of TEO to CWT-PFWs cannot well suppress its global trends and the resulting Teager energy cannot be used for damage identification. To address this problem, a two-phase local anomalies intensification method is proposed: CWT-CPFWs be calculated to suppress the global trends of 2D-CPFW and then TEO be applied to further suppress the trends and intensify the local anomalies.

2.2.1. Local anomalies intensification using CWT-CPFWs

Local anomalies intensified using CWT have been used in vibration shapes, including mode shapes [35], operational deflection shape [36] and curvature mode shapes [37]. The choice of a wavelet function in the CWT should be based on the characteristic of the vibration shapes to be analyzed and the effects of damage on the shapes [35]. Hence, there does not exist a universally appropriate wavelet function for all different vibration shapes and damage scenarios [38].

In this work, 2D-CWT with the rth-order Laplacian of Gaussian function is used to suppress the global trends of 2D-CPFW and intensify the local anomalies, which can be expressed by [31]

$$\widehat{\kappa}_t(u,v,s) = \int_{-\infty}^{\infty}\int_{-\infty}^{\infty} \Delta W_t(x,y)\,\Delta^r g_{u,v,s}(x,y)\,\mathrm{d}x\mathrm{d}y = \left(\Delta^r \tilde{g}_s \otimes \Delta W_t\right)(u,v) \tag{13}$$

where r is a non-negative integer and $2r$ is defined as the number of vanishing moments of $\Delta^r\tilde{g}_s$. When $r=0$, $\widehat{\kappa}_t(u,v,s)$ is proportional to $\widehat{W}_t(u,v,s)$ in Eq. (12), i.e.,

$$\widehat{\kappa}_t(u,v,s) = \left(\tilde{g}_s \otimes \Delta W_t\right)(u,v) \quad = \frac{1}{s^2}\widehat{W}_t(u,v,s) \tag{14}$$

When $r \geqslant 1$, based on Eq. (A.5), one has

$$\left(\Delta^r \tilde{g}_s \otimes x^\beta y^{\alpha-\beta}\right)(u,v) = 0 \tag{15}$$

where α and β are both non-negative integers with

$$0 \leqslant \beta \leqslant \alpha < 2r \tag{16}$$

Further, it can be seen that $\Delta^r\tilde{g}_s$ is orthogonal to any $(2r-1)$th-order bi-variate polynomial, which can be expressed by

$$P(x,y) = \sum_{\alpha=0}^{2r-1}\sum_{\beta=0}^{\alpha} a_{\beta,\alpha-\beta}x^\beta y^{\alpha-\beta} \tag{17}$$

where $a_{\beta,\alpha-\beta}$ denotes the coefficient of the term $x^\beta y^{\alpha-\beta}$ in the polynomial, and the orthogonality can be expressed by

$$\left(\Delta^r \tilde{g}_s \otimes P\right)(u,v) = 0 \tag{18}$$

Since $\Delta^r\tilde{g}_s$ has a finite non-zero interval, the interval of integration of the double integration in the convolution in Eq. (13) can be replaced by the non-zero interval of $\Delta^r\tilde{g}_s$. The mechanism of suppressing global trends of 2D-CPFW with proper choices of s and r in Eq. (13) can be explained based on Eq. (18). When s in $\Delta^r\tilde{g}_s$ is a fixed value, the non-zero interval of $\Delta^r\tilde{g}_s$ can be determined. When the center of $\Delta^r\tilde{g}_s$ is translated to the position (u,v), one can well fit the global trend of 2D-CPFW within the non-zero interval using a $(2r-1)$th-order bi-variate polynomial in Eq. (17). Since the order of the polynomial is smaller than $2r$, the fitted global trend of 2D-CPFW within the interval can be well suppressed by convolution with $\Delta^r\tilde{g}_s$ due to the orthogonality in Eq. (18). More importantly, as the global trends are suppressed, the local anomalies are retained and manifested. When PFW results from an excitation with finite frequency components, the maximum wavelength of PFW is constant and there exist a maximum order with which bi-variate polynomials can well fit its global trends in any finite intervals. Therefore, there exist a minimum value of r for $\Delta^r\tilde{g}_s$ with which the global trends of 2D-CPFWs can be well suppressed and the local anomalies in 2D-CPFWs can be well manifested. Further, based on the differentiation property of convolution, one has

$$\widehat{\kappa}_t(u,v,s) = \left(\Delta^r\tilde{g}_s \otimes \Delta W_t\right)(u,v) = \left(\tfrac{1}{s^2}\Delta^{r+1}\tilde{g}_s \otimes W_t\right)(u,v) \tag{19}$$

The determination of the proper value of r in Eq. (13) can be achieved by determining the minimum value of $2r+1$, with which $(2r+1)$th-order bi-variant polynomials that can well fit the global trends of PFW within a non-zero interval of $\Delta^{r+1}\tilde{g}_s$. It is worth noting that $\tilde{g}_s$ and its derivatives have the same non-zero interval.

In practice, damage identification is performed with discrete PFW and $\tilde{g}_s$ is generated on a discrete grid. The non-zero interval can be defined as a square grid with a side length of $\lceil 4s+3 \rceil$, where $\lceil\cdot\rceil$ denotes rounding a number up to the nearest integer, discrete points so that the number of points in such a non-zero interval is $\lceil 4s+3 \rceil^2$. For one bi-variant polynomial fitting $\tilde{W}_t$ that is

extracted from PFW within a finite interval centered at (u, v) of the size same as that of the non-zero interval of $\tilde{g}_s$, the polynomial can be expressed by [34]

$$\tilde{W}_t^p(x, y) = \sum_{\alpha=0}^{d(u,v)} \sum_{\beta=0}^{\alpha} c_{\beta,\alpha-\beta}(u, v)\, x^{\beta} y^{\alpha-\beta} \tag{20}$$

where $d(u, v)$ and $c_{\beta,\alpha-\beta}(u, v)$ denote the order and coefficients of the polynomial, respectively. To determine a proper value of $d(u, v)$, the modal assurance criterion between $\tilde{W}_t$ and $\tilde{W}_t^p$ is used, which can be calculated by [39]

$$\mathrm{MAC}(\varphi, \varphi^p) = \frac{\left((\varphi^p)^{\mathrm{T}} \varphi\right)^2}{\left((\varphi^p)^{\mathrm{T}} \varphi^p\right)\left((\varphi)^{\mathrm{T}} \varphi\right)} \times 100\% \tag{21}$$

where φ and φ^p denote the column-vectorization of $\tilde{W}_t$ and $\tilde{W}_t^p$, respectively, and the superscript T denotes matrix transpose. The proper value of d is equal to the minimum order of the polynomial with which MAC is greater than 90%. After exhaustively roving the extraction of $\tilde{W}_t$ over the PFW, the proper orders of all the bi-variant polynomials associated with PFW at all measurement points are obtained. While the PFW corresponds to multiple instants are usually available, a three-dimensional spatial–temporal matrix $\mathbf{d}$ containing d associated with a number of instants can be obtained. In this paper, the number of instants is same as that used to calculate a damage index based on CWT-PFW, which is discussed in Section 2.3.

Since high values of d caused by measurement noise can exist in certain (u, v) and t, a statistical criterion is applied to assist determination of the proper value of r based on all entries of $\mathbf{d}$. The upper bound of two standard deviations of the mean for $\mathbf{d}$ is calculated as

$$\tau = \mu + 2\sigma \tag{22}$$

where μ and σ denote the mean and standard deviation of all the entries of $\mathbf{d}$, respectively. In the criterion, $2r + 1$ should not be smaller than τ so that the proper value of r for $\Delta^r \tilde{g}_s$ to suppress the global trends of 2D-CPFW is expressed by

$$r = \left\lceil \frac{\tau - 1}{2} \right\rceil \tag{23}$$

Note that values of the 97.7% entries of $\mathbf{d}$ are not greater than τ [40], assuming that values the entries well spread in a normal distribution, and the criterion can effectively rule out the outliers in $\mathbf{d}$ when determining the proper value of r.

2.2.2. Local anomalies intensification using TEO

TEO was first proposed to estimate the point-wise energy of a one-dimensional oscillating discrete signal p. It is a nonlinear operator and can be expressed by [41]

$$\Psi(p[n]) = p^2[n] - p[n-1]\, p[n+1] \tag{24}$$

where $p[n]$ denotes the value of p at point n. TEO was later extended to handle a 2D discrete signal q [42], and the 2D TEO can be expressed by

$$\begin{aligned} \Psi^{2\mathrm{D}}(q[n, m]) &= q^2[n, m] - q[n-1, m]\, q[n+1, m] + q^2[n, m] - q[n, m-1]\, q[n, m+1] \\ &= 2q^2[n, m] - q[n-1, m]\, q[n+1, m] - q[n, m-1]\, q[n, m+1] \end{aligned} \tag{25}$$

where $q[n, m]$ denotes the value of q at points $[n, m]$. It has been shown that Ψ and $\Psi^{2\mathrm{D}}$ can intensify weak local anomalies of curvature mode shapes [19,37]. It is proposed that the $\Psi^{2\mathrm{D}}$ be applied to CWT-PFW and CWT-CPFW for intensifying local anomalies caused by damage and identifying its location: Teager energy of CWT-PFW and that of CWT-CPFW can be expressed by

$$\Psi^{2\mathrm{D}}\left(\widehat{W}_t[n, m]\right) = 2\left(\widehat{W}_t[n, m]\right)^2 - \widehat{W}_t[n-1, m]\, \widehat{W}_t[n+1, m] - \widehat{W}_t[n, m-1]\, \widehat{W}_t[n, m+1] \tag{26}$$

and

$$\Psi^{2\mathrm{D}}\left(\widehat{\kappa}_t[n, m]\right) = 2\left(\widehat{\kappa}_t[n, m]\right)^2 - \widehat{\kappa}_t[n-1, m]\, \widehat{\kappa}_t[n+1, m] - \widehat{\kappa}_t[n, m-1]\, \widehat{\kappa}_t[n, m+1] \tag{27}$$

respectively, where $\widehat{W}_t[n, m]$ and $\widehat{\kappa}_t[n, m]$ denote the discrete values of CWT-PFW and CWT-CPFW at $[n, m]$, respectively.

2.3. Damage identification based on intensified anomalies

When one mode shape is used for damage identification, it can be insensitive to certain damage or it cannot fully indicate the extent of the damage. In this case, uses of other mode shapes are necessary as the more mode shapes are used, the more likely the location and extent of the damage are identified. Similarly, not all Teager energy of CWT-CPFWs with different instants described in Section 2.2 can fully indicate the location and extent of damage, and each of them may be able to indicate a fraction of the extent of the damage. While it is advantageous that a relatively large number of waveforms are usually measured, an accumulative damage index based on Teager energy of CWT-CPFW is proposed and expressed by

$$\delta\left(\Psi^{2\mathrm{D}}\left(\widehat{\kappa}_t[n, m]\right)\right) = \sum_{t=t_1}^{t=t_2} \left|\Psi^{2\mathrm{D}}\left(\widehat{\kappa}_t[n, m]\right)\right| \tag{28}$$

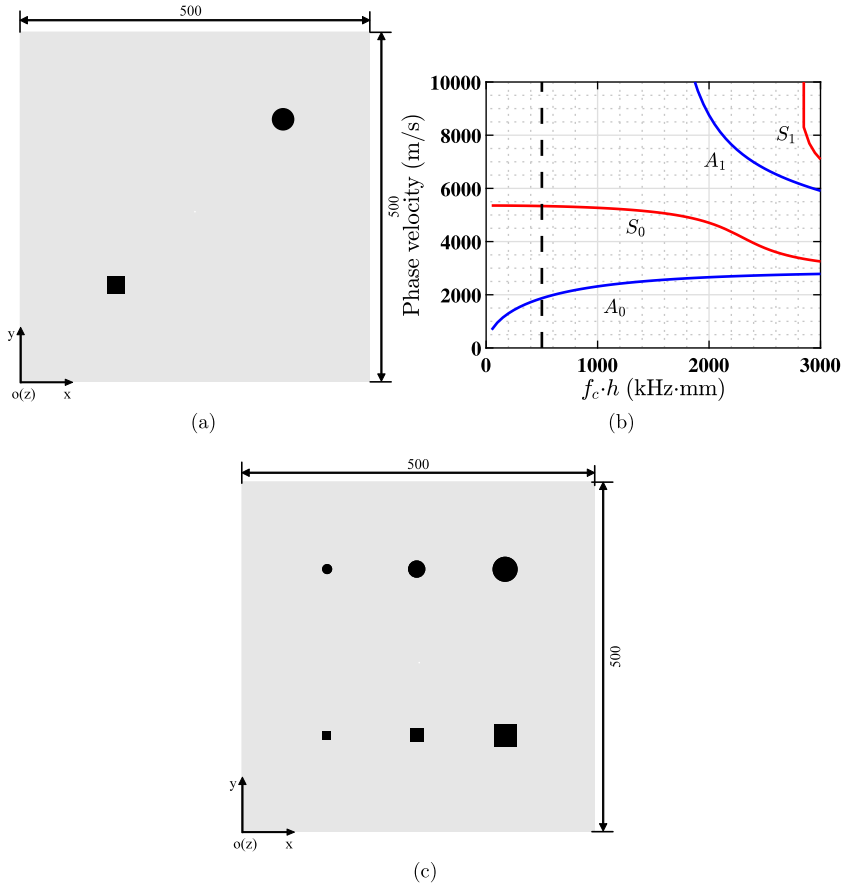

Fig. 1. (a) Dimensions of specimen #1 with damage in the form of two thickness reduction areas (unit: mm), (b) phase velocity dispersion curves of specimen #1, and (c) dimensions of specimen #2 with damage in the form of six thickness reduction areas (unit: mm). Locations and extent of square and circular damage areas are depicted by solid black areas in (a) and (c). The dotted line in (b) corresponds to the value of frequency-thickness product with $f_c = 50$ kHz.

where t_1 and t_2 are the starting and ending instants of waveforms to be included in δ, and $|\cdot|$ denotes an absolute value. The effectiveness of δ for identifying the location and extent of damage depends on values of t_1 and t_2, which determine waveforms to be included. Since the use of waveforms near an excitation point can lead to misdiagnosis as local anomalies [23], t_1 should be selected as an instant after the excitation ends. In this work, it is proposed that the proper value of t_1 be

$$t_1 = t_e + t_p \tag{29}$$

where t_e and t_p denote the ending instant and duration of the excitation, respectively. The inclusion of t_p in Eq. (29) can diminish misdiagnosis due to the large-magnitude waveforms generated during the occurrence of the excitation. Regarding the proper value of t_2, it is proposed that the value be determined based on a convergence index denoted by conv, and its value at the ith iteration is expressed by

$$\text{conv}\,(i) = \frac{\|\delta_i\|_2}{\|\delta_i\|_2 + \|\delta_i - \delta_{i+1}\|_2} \tag{30}$$

where $\|\cdot\|_2$ denotes the 2-norm of a vector, δ_i and δ_{i+1} are calculated using δ in Eq. (28) with the same value of t_1 in Eq. (29) but different values of t_2 for δ_i and δ_{i+1} in Eq. (30), which are calculated by

$$t_2 = t_1 + \frac{ik}{f_s} \tag{31}$$

and

$$t_2 = t_1 + \frac{(i+1)\,k}{f_s} \tag{32}$$

respectively, in which k denotes the incremental number of waveforms for one iteration and f_s denotes the sampling frequency of the waveforms. On one hand, δ with a larger value of t_2 may lead to a more complete identification of the extent of the damage,

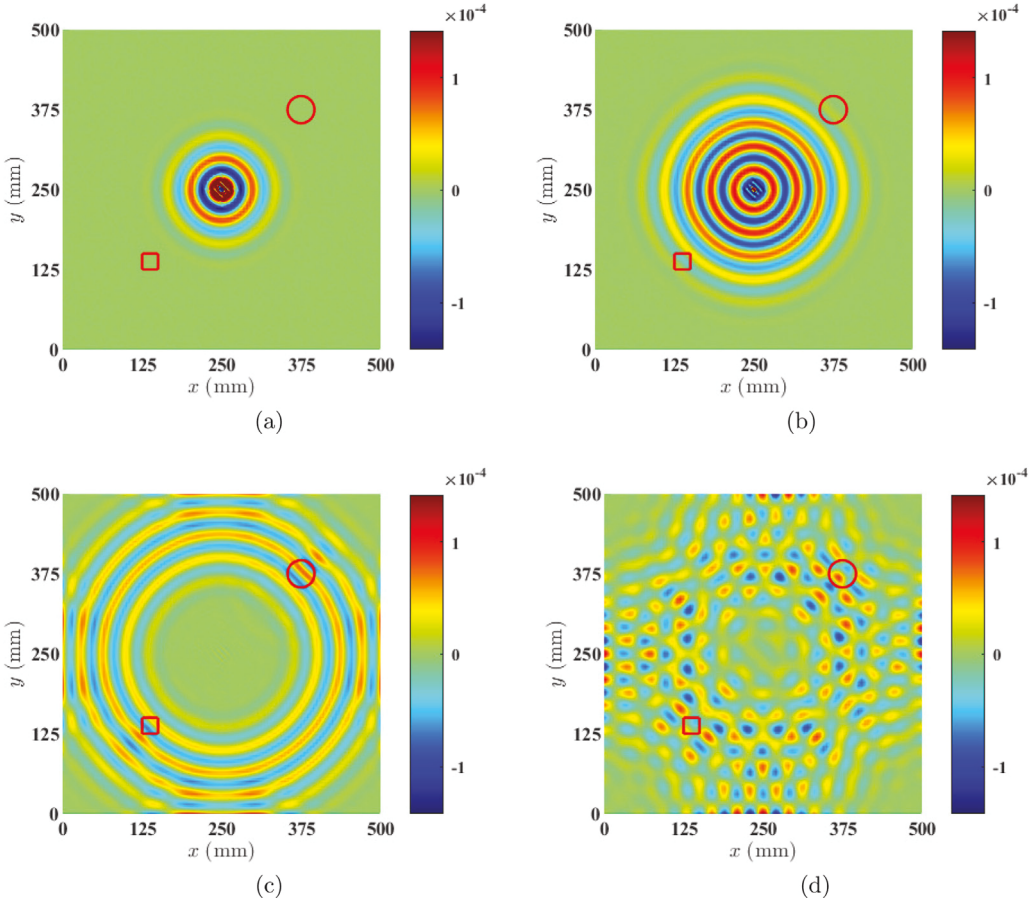

Fig. 2. Waveforms of the PFWs at (a) 50 μs, (b) 80 μs, (c) 120 μs, and (d) 275 μs. Locations and extent of the square and circular damage areas are depicted by solid red lines.

since δ cumulatively collects anomalies caused by the damage. Further, when t_2 is increased to a certain value, δ will converge and so will its associated damage identification result. On the other hand, since a high sampling frequency is usually used to measure waveforms in practice, changes of δ between two consecutive sampling instants can be so small that a false convergence can be achieved. As a result, it leads to a trivial conv and inaccurate damage identification results. Hence, k is introduced to t_2 in Eqs. (31) and (32) in order to include multiple waveforms to better quantify the convergence of δ. In this work, the value of k is chosen as 5 and 30 in the numerical and experimental investigations, respectively, and the proper value of t_2 is chosen as its minimum value, with which conv $\geqslant 0.99$.

To quantitatively evaluate identification results from the proposed method, a percentage energy ratio is formulated as

$$\chi = \frac{\sum\limits_{\text{damage area(s)}} \delta^2}{\sum\limits_{\text{whole area}} \delta^2} \times 100\% \tag{33}$$

where $\sum\limits_{\text{damage area(s)}} \delta$ and $\sum\limits_{\text{whole structure}} \delta$ calculate summations of δ^2 over damage and whole inspected areas, respectively. It is worth noting that $\chi \in [0, 100\%]$ and a higher χ value indicates a better damage identification result with a lower disturbance from measurement noise/errors beyond the damage area(s). In addition, $\delta\left(\widehat{W}_t\right)$ and $\delta\left(\Psi^{2\mathrm{D}}\left(\widehat{W}_t\right)\right)$ are obtained by replacing $\Psi^{2\mathrm{D}}\left(\widehat{\kappa}_t\right)$ in Eq. (28) with $\widehat{W}_t$ and $\Psi^{2\mathrm{D}}\left(\widehat{W}_t\right)$ for comparison purposes, respectively, and RMS values based $W_t[n,m]$ can also be used for comparison purposes and considered another type of damage index. It can be expressed by [23]

$$\mathrm{RMS}\left(W_t[n,m]\right) = \sqrt{\frac{\sum_{t=t_1}^{t=t_2}\left(W_t[n,m]\right)^2}{\left(t_2 - t_1\right) f_s}} \tag{34}$$

where the value of t_1 can be obtained from Eq. (29) and that of t_2 can be estimated Eq. (30) by replacing δ with RMS, and damage identification results based on RMS can also be evaluated using χ in (33) by replacing δ with RMS. So far, four different damage

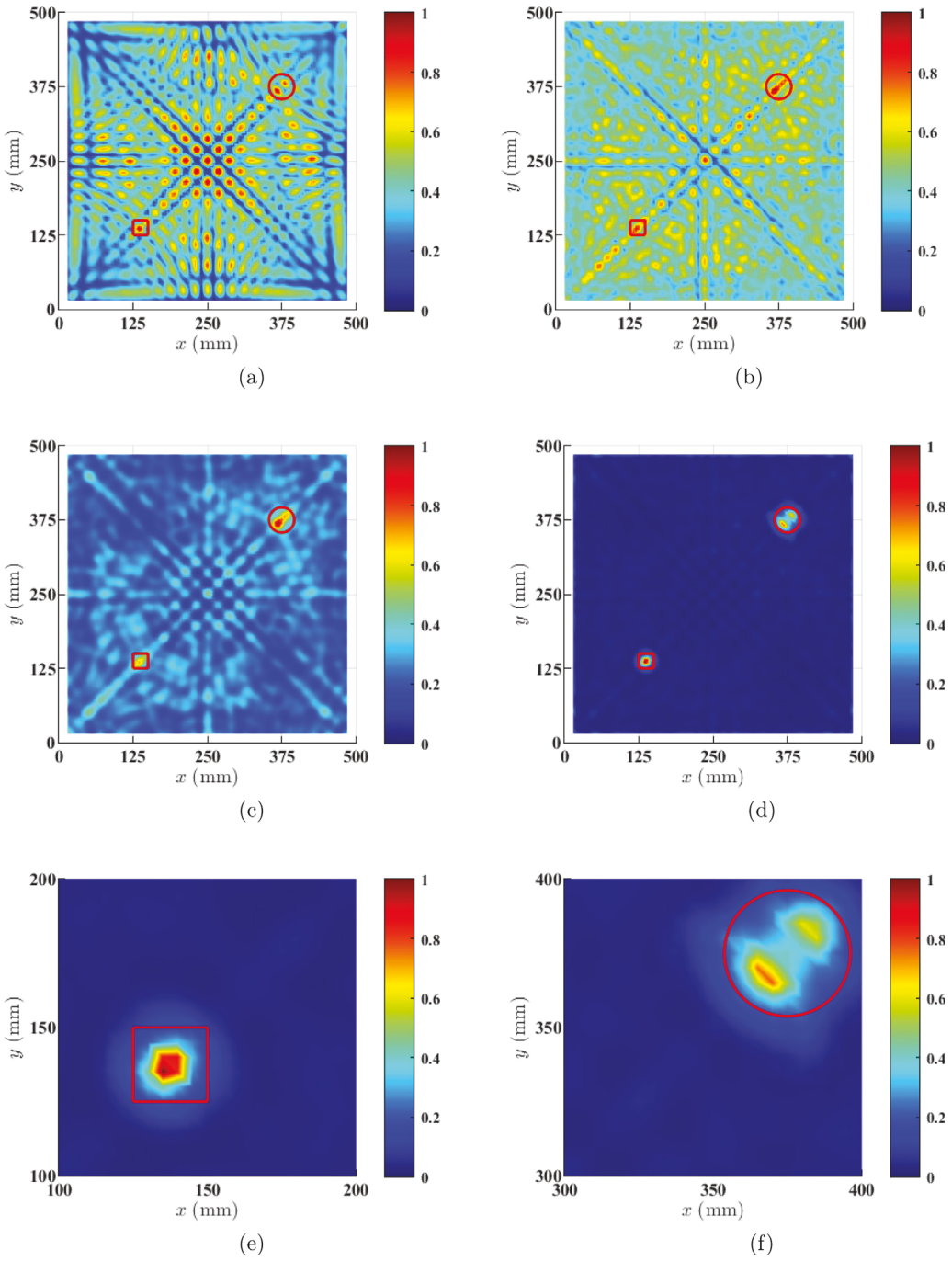

Fig. 3. Damage identification results for the specimen #1 based on (a) RMS (W_t), (b) $\delta\left(\widehat{W}_t\right)$, (c) $\delta\left(\Psi^{2D}\left(\widehat{W}_t\right)\right)$, (d) $\delta\left(\Psi^{2D}\left(\widehat{\kappa}_t\right)\right)$, (e) a zoomed-in view of the square damage area in (d), and (f) a zoomed-in view of the circular damage area in (d). Locations and extent of square and circular damage areas are depicted by solid red lines. For better comparison, the damage index values shown in each figure are normalized so that their maximum value is equal to one.

indexes $\delta\left(\Psi^{2D}\left(\widehat{\kappa}_t\right)\right)$, $\delta\left(\widehat{W}_t\right)$, $\delta\left(\Psi^{2D}\left(\widehat{W}_t\right)\right)$ and RMS (W_t) are defined. Their effectiveness and robustness for damage identification will be numerically and experimental investigated and compared in Sections 3 and 4.

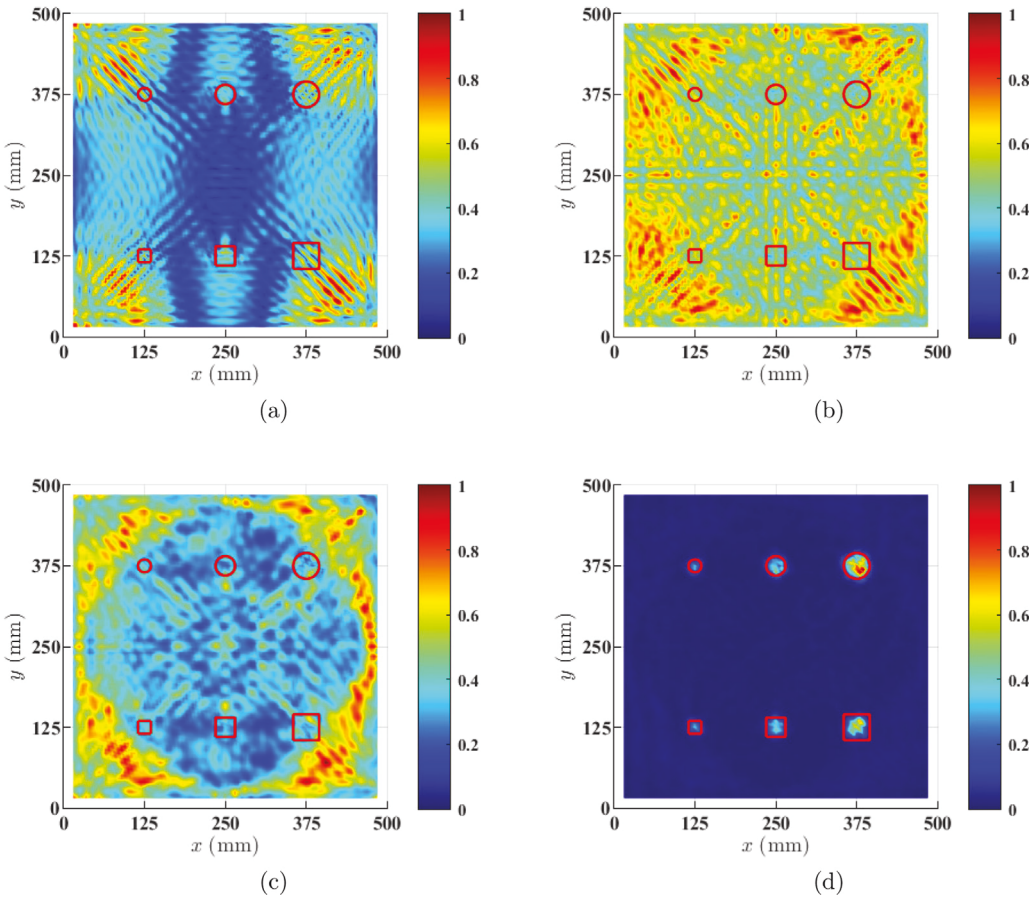

Fig. 4. Damage identification results of the specimen #2 based on (a) RMS (W_t), (b) $\delta\left(\widehat{W}_t\right)$, (c) $\delta\left(\Psi^{2D}\left(\widehat{W}_t\right)\right)$, and (d) $\delta\left(\Psi^{2D}\left(\widehat{\kappa}_t\right)\right)$. Locations and extent of square and circular damage areas are depicted by solid red lines. For better comparison, the damage values shown in each figure are normalized so that their maximum value is equal to one.

3. Numerical investigations

In this section, the effectiveness and noise-robustness of the proposed method are investigated using numerical simulations of two aluminum plates, specimen #1 and #2, with damage. The specimen #1 has damage in the form of two thickness reduction areas and the specimen #2 has damage in the form of six thickness reduction areas.

3.1. Numerical simulation of specimen #1

The specimen #1, a free-free-free-free aluminum plate of a thickness 10 mm is simulated with dimensions shown in Fig. 1(a). Its mass density is 2700 kg/m^3, Young's modulus is 69 GPa, and Poisson's ratio is 0.33. A finite element model of the specimen #1 is constructed using ABAQUS with linear eight-node brick (C3D8R) elements. Two one-sided thickness reduction areas, including a square one and a circular one, with a depth of 1 mm are introduced to the plate. The square damage and circular damage areas are centered at $(137.5, 137.5)$ mm and $(375, 375)$ mm, respectively; the square damage area has a side length of 25 mm and the circular damage area has a radius of $15\sqrt{2}$ mm. The specimen #1 is under zero initial conditions and subject to an excitation force applied to its central location, i.e., $(250, 250)$ mm. The force is an N_c-count wave packet that can be analytically expressed by [8]

$$f(t) = A\left(H(t) - H\left(t - \frac{N_c}{f_c}\right)\right)\left(1 - \cos\left(\frac{2\pi f_c t}{N_c}\right)\right)\sin\left(2\pi f_c t\right) \tag{35}$$

where A denotes the magnitude of f, H is Heaviside function, which is expressed by

$$H(t) = \begin{cases} 1, & t \geqslant 0 \\ 0, & t < 0 \end{cases} \tag{36}$$

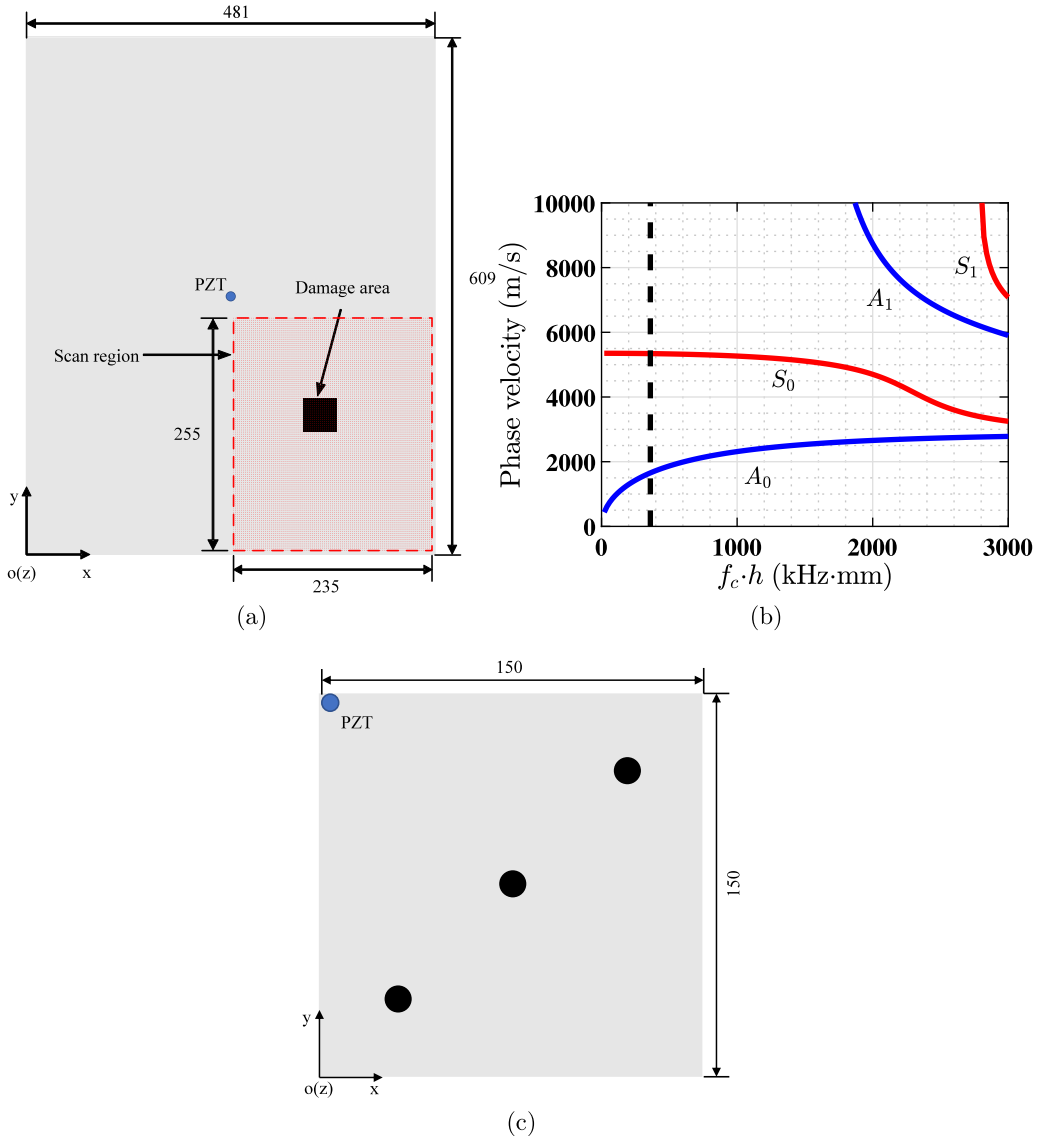

Fig. 5. (a) Dimensions of the specimen #3 with damage in the form of a square 10% thickness reduction area, and an assigned scan region for SLDV measurements (unit: mm), (b) phase velocity dispersion curves of the specimen #3, and (c) dimensions of the specimen #4 with damage in the form of three circular 50% thickness reduction areas (unit: mm). Locations and extent of damage areas are depicted by solid black areas in (a) and (c). The dotted line in (b) corresponds to the largest frequency-thickness product associated with all f_c and thickness of the two specimens in the experimental investigations.

and f_c is the central frequency of the force. In this numerical example, the applied excitation force is a five-count wave packet with $A = 0.5$ N, $N_c = 5$ and $f_c = 50$ kHz. Phase velocity dispersion curves of the specimen #1 are shown in Fig. 1(b). It can be seen that only S0 and A0 Lamb wave modes exist at the frequency-thickness product 500 kHz · mm associated with $f_c = 50$ kHz.

Waveforms of PFWs of the specimen #1 are obtained on a grid of 101 × 101 measurement points with a sampling frequency of 2 MHz for the first 5 ms after the excitation is applied; a total of 10001 waveforms are obtained. To investigate effects of measurement noise on damage identification results, white Gaussian noise is added to the PFWs of the specimen #1 such that a signal-to-noise ratio (SNR) of 30 dB is achieved. Figs. 2(a) through (d) show four noise-contaminated waveforms at 50 μs, 80 μs, 120 μs and 275 μs, respectively. In Fig. 2(a), a PFW is generated and spreads out from the excitation point, and its wavefront can be observed. In Fig. 2(b), the wavefront of the PFW is traveling through the two damage areas but wave reflections cannot be detected. In Fig. 2(c), the wavefront is beyond the two damage areas and the PFW is reflected from the two damage areas, but the reflections are not imminent. Subsequently, as shown in Fig. 2(d), distinct wave propagation features related to the damage are not noticeable, as they are masked by those related to reflections of the waves at the boundaries.

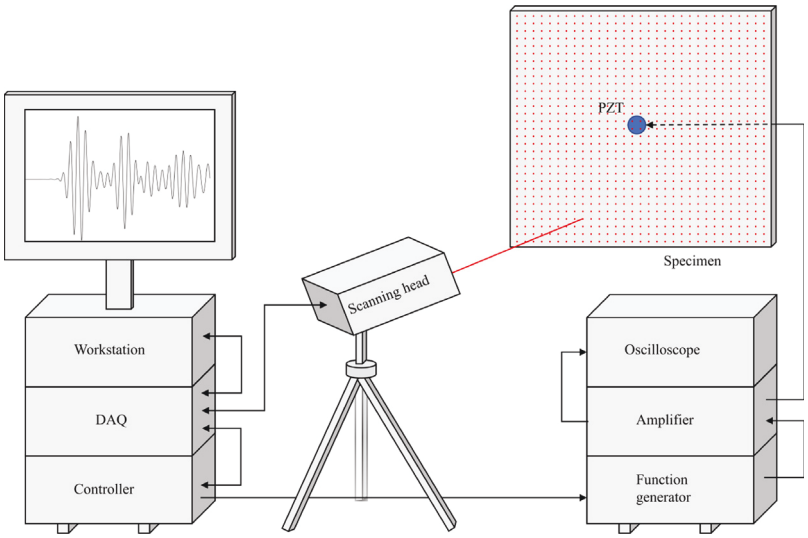

Fig. 6. Schematic of the experimental setup.

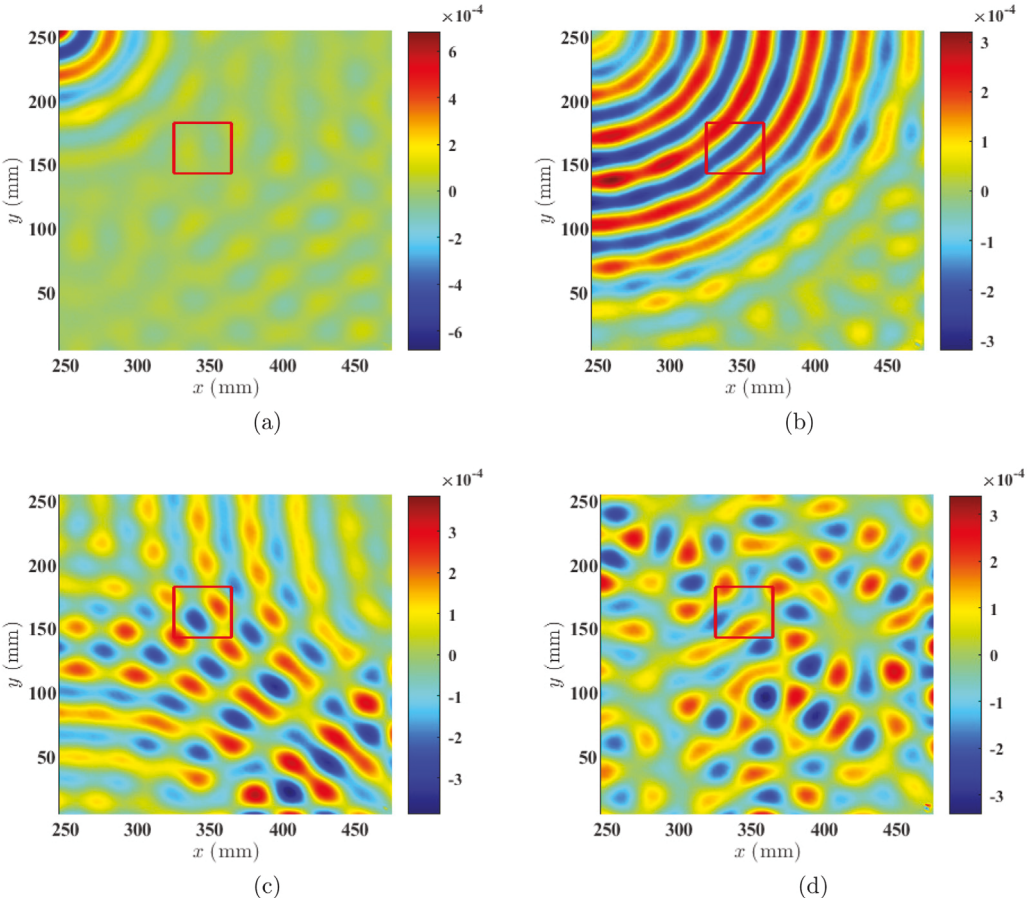

Fig. 7. Waveforms of the PFWs in the specimen #3 associated with $f_c = 30$ kHz at (a) 280 μs, (b) 360 μs, (c) 480 μs, and (d) 1200 μs. The location and extent of the damage are depicted by solid lines.

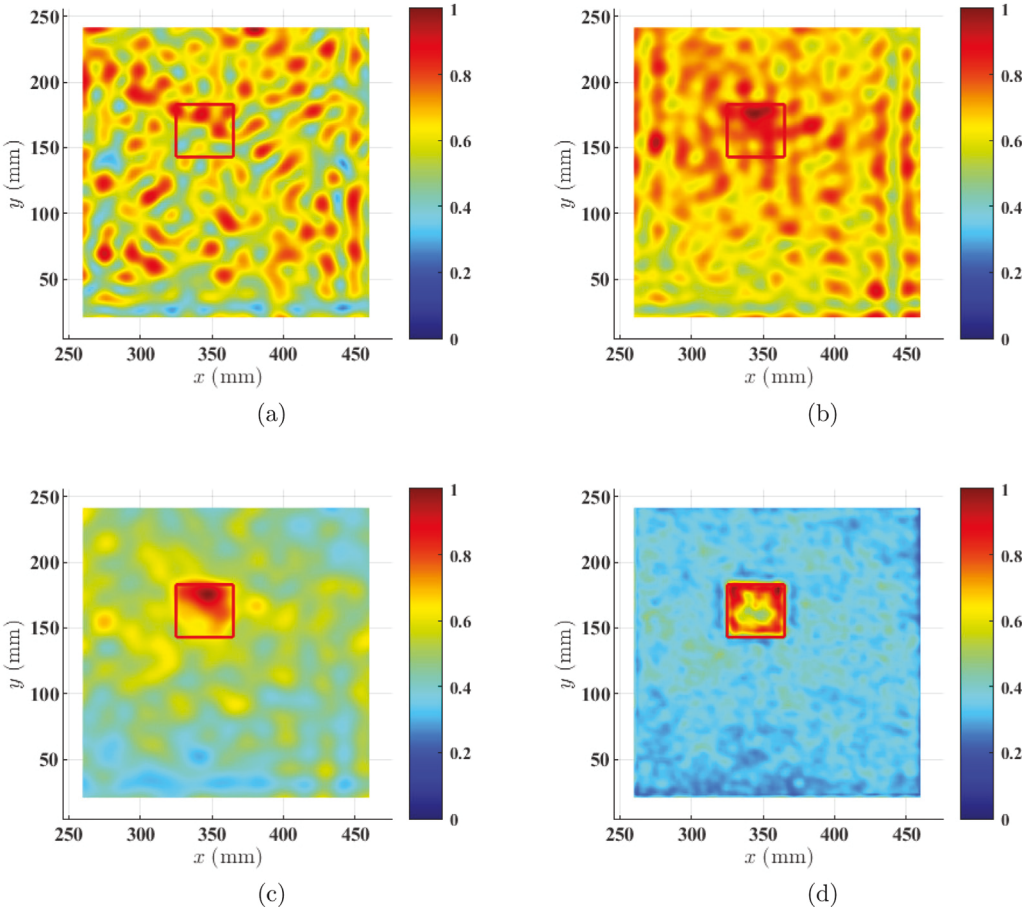

Fig. 8. Damage identification results of the specimen #3 with f_c = 30 kHz based on (a) RMS (W_t), (b) $\delta\left(\widehat{W}_t\right)$, (c) $\delta\left(\Psi^{2D}\left(\widehat{W}_t\right)\right)$, and (d) $\delta\left(\Psi^{2D}\left(\hat{\kappa}_t\right)\right)$. The location and extent of the damage area are depicted by solid red lines. For better comparison, the damage values shown in each figure are normalized so that their maximum value is equal to one.

3.2. Damage identification results and discussion for specimen #1

The proposed damage identification method is applied to identify the damage on the specimen #1. The value of s for $\delta\left(\widehat{W}_t\right)$, $\delta\left(\Psi^{2D}\left(\widehat{W}_t\right)\right)$ and $\delta\left(\Psi^{2D}\left(\hat{\kappa}_t\right)\right)$ is selected to be 2 and the proper value of r for $\delta\left(\Psi^{2D}\left(\hat{\kappa}_t\right)\right)$ is determined to be 3 based on Eq. (23). Damage indexes RMS (W_t), $\delta\left(\widehat{W}_t\right)$, $\delta\left(\Psi^{2D}\left(\widehat{W}_t\right)\right)$ and $\delta\left(\Psi^{2D}\left(\hat{\kappa}_t\right)\right)$ are calculated and shown in Figs. 3(a) through (d), respectively. In Fig. 3(a), large index values are observed within and beyond the two damage areas, and those in the latter lead to false positive identification of the locations and extent of the damage. A similar observation can be made for $\delta\left(\widehat{W}_t\right)$ in Fig. 3(b). It is difficult to identify the damage locations and extent based on RMS (W_t) and $\delta\left(\widehat{W}_t\right)$. In Fig. 3(c), large index values can be observed within the neighborhoods of the two damage areas, but relatively large index values can also be observed beyond the damage areas. It is because TEO can only partially suppress global trends of $\widehat{W}_t$. In Fig. 3(d), $\delta\left(\Psi^{2D}\left(\hat{\kappa}_t\right)\right)$ has the best identification result: large index values can only be observed within the neighborhoods of the two damage areas. Specifically, as shown in Figs. 3(e) and (f), large index values only exist within the damage areas. Therefore, 2D-CWT with the third-order Laplacian of Gaussian function can well suppress global trends of $\widehat{W}_t$. Energy ratios χ associated with RMS (W_t), $\delta\left(\widehat{W}_t\right)$, $\delta\left(\Psi^{2D}\left(\widehat{W}_t\right)\right)$ and $\delta\left(\Psi^{2D}\left(\hat{\kappa}_t\right)\right)$ are 2.0%, 2.3%, 4.9% and 51.2%, respectively, and damage identification results obtained from $\delta\left(\Psi^{2D}\left(\hat{\kappa}_t\right)\right)$ are better than those from RMS (W_t), $\delta\left(\widehat{W}_t\right)$ and $\delta\left(\Psi^{2D}\left(\widehat{W}_t\right)\right)$.

3.3. Numerical simulation and damage identification for specimen #2

The specimen #2 is studied to validate the effectiveness of the proposed damage identification method for damage areas with relatively small sizes than those in the specimen #1. The specimen #2 is made of the materials same as those of the specimen #1,

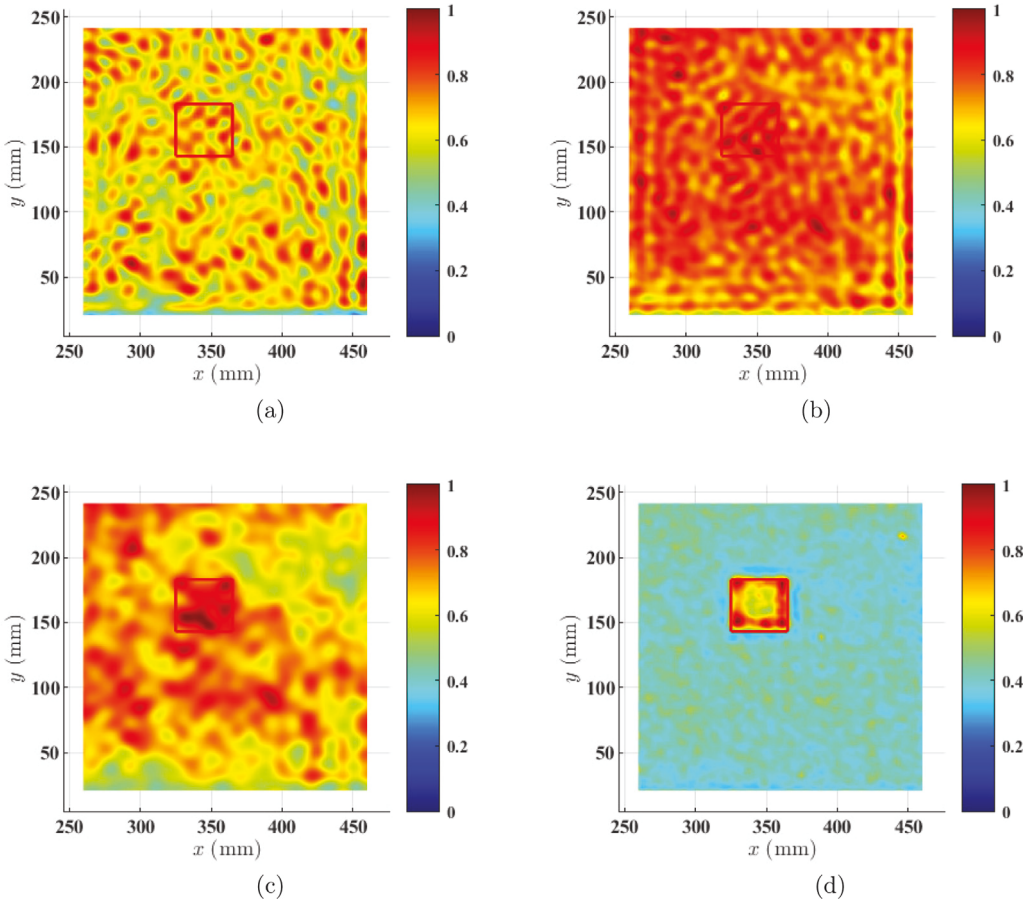

Fig. 9. Damage identification results of the specimen #3 with f_c = 50 kHz based on (a) RMS (W_t), (b) $\delta\left(\widehat{W}_t\right)$, (c) $\delta\left(\Psi^{2D}\left(\widehat{W}_t\right)\right)$, and (d) $\delta\left(\Psi^{2D}\left(\hat{\kappa}_t\right)\right)$. The location and extent of the damage area are depicted by solid red lines. For better comparison, the damage values shown in each figure are normalized so that their maximum value is equal to one.

its dimensions and boundary conditions are the same as those of the specimen #1. The specimen has damage in the form of six thickness reduction areas: three square damage areas centered at $(125, 125)$ mm, $(250, 125)$ mm and $(375, 125)$ mm with side lengths of 20 mm, 25 mm and 30 mm, respectively and three circular ones centered at $(125, 375)$ mm, $(250, 375)$ mm and $(375, 375)$ mm with radii of 10 mm, 15 mm and 20 mm, respectively. Each damage area has a 1-mm one-sided thickness reduction. Dimensions and locations of the damage areas can be found in Fig. 1(c). The excitation force is the same as that used for the specimen #1 and applied to the center of the specimen #2. Waveforms of PFWs of the specimen #2 are obtained on a grid of 101×101 measurement points with a sampling frequency of 2 MHz for the first 1.5 ms after the excitation is applied; a total of 3001 waveforms are obtained. White Gaussian noise is added to the PFWs of the specimen #2 such that a SNR of 30 dB is achieved. Besides, the phase velocity dispersion curves of the specimen #2 are same to those in the specimen #1, as they are made of the same materials and their undamaged portions have the same thickness. Hence only S0 and A0 Lamb wave modes exist at the frequency-thickness product same as that for the specimen #1.

The proposed damage identification method is applied to identify the damage on the specimen #2. The value of s for $\delta\left(\widehat{W}_t\right)$, $\delta\left(\Psi^{2D}\left(\widehat{W}_t\right)\right)$ and $\delta\left(\Psi^{2D}\left(\hat{\kappa}_t\right)\right)$ is selected to be 2 and the proper value of r for $\delta\left(\Psi^{2D}\left(\hat{\kappa}_t\right)\right)$ is determined to be 3 based on Eq. (23). Damage indexes RMS (W_t), $\delta\left(\widehat{W}_t\right)$, $\delta\left(\Psi^{2D}\left(\widehat{W}_t\right)\right)$ and $\delta\left(\Psi^{2D}\left(\hat{\kappa}_t\right)\right)$ are calculated and shown in Figs. 4(a) through (d), respectively. In Fig. 4(a), large index values are observed within and beyond the six damage areas, and those in the latter lead to false positive identification results of the locations and extent of the damage. Large index values cannot be observed within the neighborhoods of the damage in $\delta\left(\widehat{W}_t\right)$ and $\delta\left(\Psi^{2D}\left(\widehat{W}_t\right)\right)$ in Figs. 4(b) and (c). Hence it is difficult to identify the damage locations and extent based on RMS (W_t), $\delta\left(\widehat{W}_t\right)$ and $\delta\left(\Psi^{2D}\left(\widehat{W}_t\right)\right)$. In Fig. 4(d), $\delta\left(\Psi^{2D}\left(\hat{\kappa}_t\right)\right)$ has the best identification result similar to that of the specimen #1. Energy ratios χ associated with RMS (W_t), $\delta\left(\widehat{W}_t\right)$, $\delta\left(\Psi^{2D}\left(\widehat{W}_t\right)\right)$ and $\delta\left(\Psi^{2D}\left(\hat{\kappa}_t\right)\right)$ are 3.8%, 2.7%, 2.2% and 73.8%, respectively and the damage identification results obtained from $\delta\left(\Psi^{2D}\left(\hat{\kappa}_t\right)\right)$ are the best.

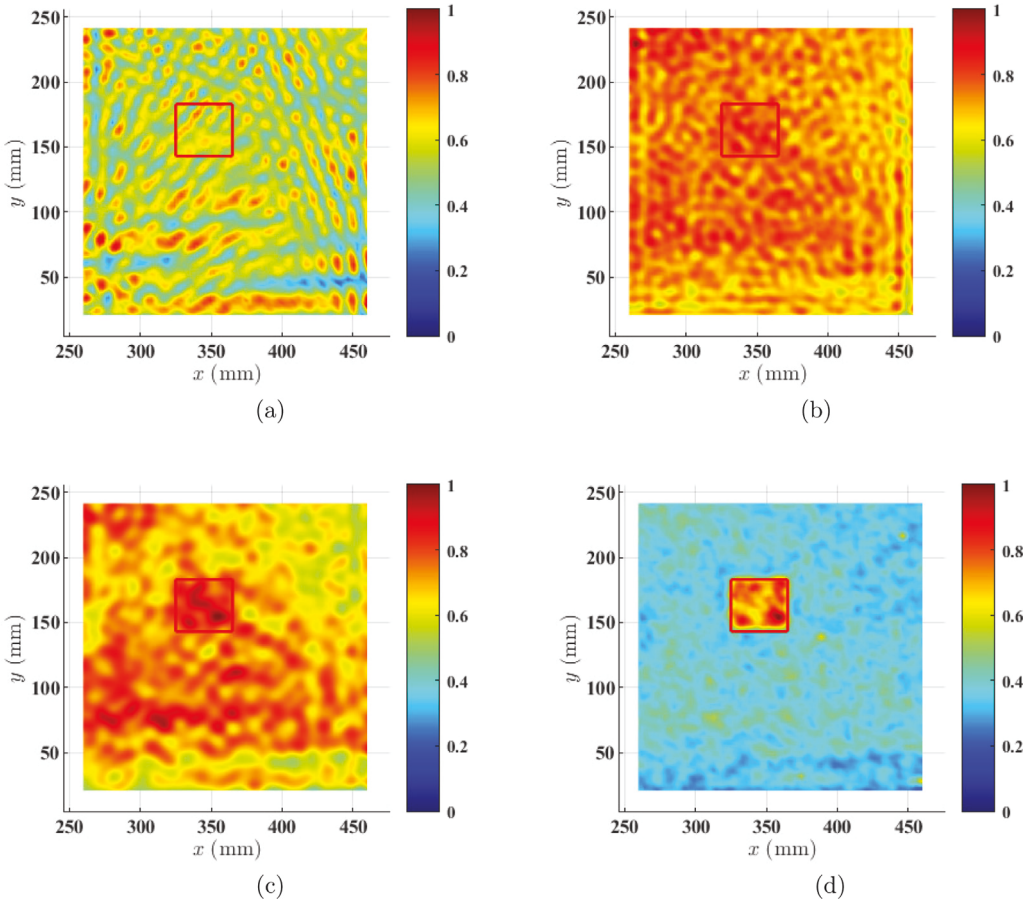

Fig. 10. Damage identification results of the specimen #3 with $f_c = 70$ kHz based on (a) RMS (W_t), (b) $\delta\left(\widehat{W}_t\right)$, (c) $\delta\left(\Psi^{2D}\left(\widehat{W}_t\right)\right)$, and (d) $\delta\left(\Psi^{2D}\left(\hat{\kappa}_t\right)\right)$. The location and extent of the damage area are depicted by solid red lines. For better comparison, the damage values shown in each figure are normalized so that their maximum value is equal to one.

4. Experimental investigations

The effectiveness of the proposed damage identification method was experimentally investigated on two aluminum plates, specimen #3 and #4. The two specimen had different dimensions, damage number, locations and extent.

4.1. Experimental test and waveform measurement for specimen #3

The specimen #3 had a length of 609 mm, a width of 481 mm, and a thickness of 4 mm. A square damage in the form of 10% thickness reduction with a side length of 40 mm was introduced to a side of the specimen #3; the damage was centered at (345, 163) mm on the specimen. Dimensions of the specimen #3 and damage area are depicted in Fig. 5(a). A schematic of the experimental setup is shown in Fig. 6. A circular lead–zirconate–titanate (PZT) actuator with a diameter of 10 mm was placed on the damaged side of the specimen #3 at $x = 240$ mm and $y = 263$ mm to generate excitation forces. The excitation forces were generated by a Tektronix AFG3022C function generator in the form of a five-count wave packet with four f_c, including 30 kHz, 50 kHz, 70 kHz and 90 kHz; the peak-to-peak amplitude of the excitation forces were amplified to 150 V for $f_c = 30$ kHz, 50 kHz and 90 kHz, and 50 V for $f_c = 70$ kHz by a Krohn-Hite 7500 amplifier, and they were fed to the PZT actuator; and a Tektronix TBS2104 oscilloscope was used to monitor the amplified excitation forces. A Polytec PSV-500-HV SLDV was employed to measure waveforms on a scan region with a length of 235 mm and a width of 255 mm assigned to the bottom right corner of the intact surface of the specimen #3 with a clearance of 5 mm from the sides of the specimen #3. A grid of 101 × 111 measurement points was defined within the scan region. A sampling frequency of 1.25 MHz was used to measure the response of each measurement point for 10 ms. For each measured response, 30 averages were carried out to minimize adverse effects of measurement errors. The averaged measured responses of all measurement points were reconstructed as 2D waveforms at each measurement instant. It was taken about two hours to finish the whole measurement process in each case of excitation force. Phase velocity dispersion curves of the specimen #3 are shown in Fig. 5(b). It can be seen that only S0 and A0 Lamb wave modes exist at all f_c.

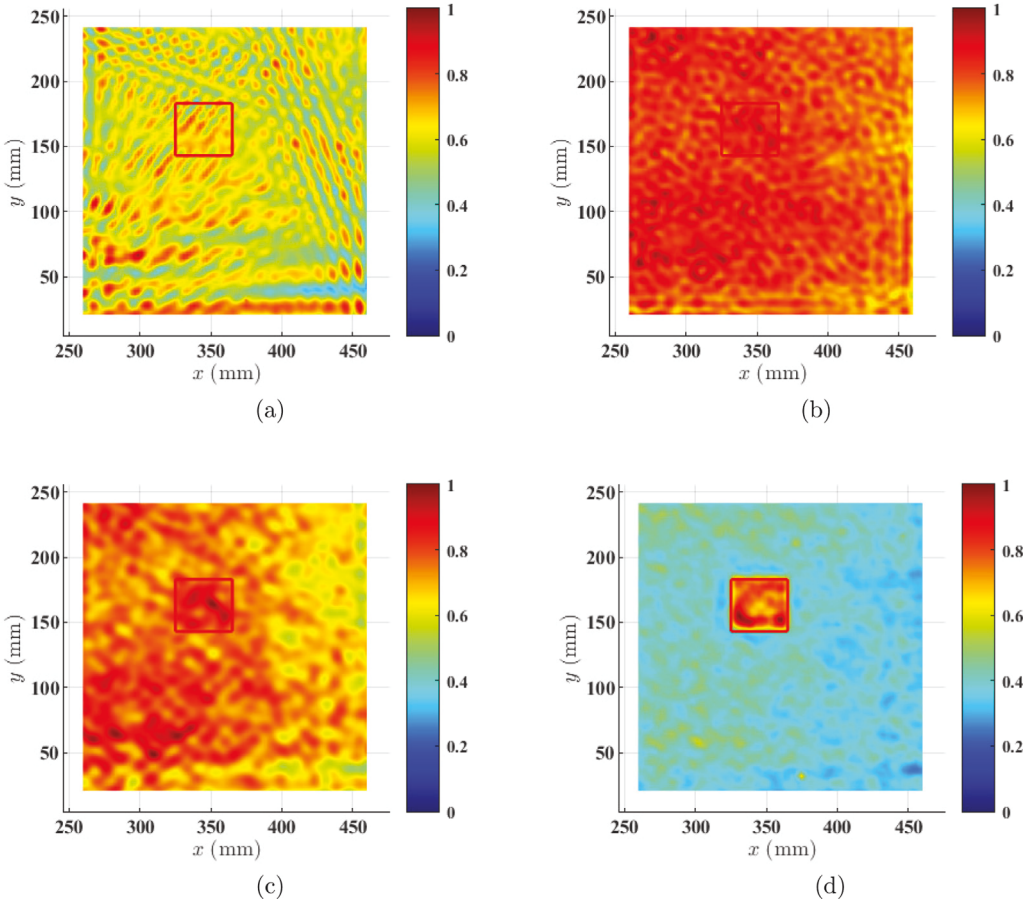

Fig. 11. Damage identification results of the specimen #3 with f_c = 90 kHz based on (a) RMS (W_t), (b) $\delta\left(\widehat{W}_t\right)$, (c) $\delta\left(\Psi^{2D}\left(\widehat{W}_t\right)\right)$, and (d) $\delta\left(\Psi^{2D}\left(\hat{\kappa}_t\right)\right)$. The location and extent of the damage area are depicted by solid red lines. For better comparison, the damage values shown in each figure are normalized so that their maximum value is equal to one.

Four waveforms of the PFWs at 280 μs, 360 μs, 480 μs and 1200 μs associated with f_c = 30 kHz are shown in Figs. 7(a) through (d), respectively. In Fig. 7(a), the PFW was generated and spread out in the form of concentric sectors. In Fig. 7(b), the wavefront of the PFW arrived near the boundaries of the specimen #3. In Fig. 7(c), the PFW reflected from the boundaries and propagated in various directions. Subsequently, the PFW was scattered as shown in Fig. 7(d). It can be observed that the PFWs were not noticeably affected by the existence of the damage.

4.2. Damage identification results and discussion for specimen #3

To validate the effectiveness of the proposed damage identification method, the waveforms of PFWs of specimen #3 associated with the four f_c were investigated. The value of s for $\delta\left(\widehat{W}_t\right)$, $\delta\left(\Psi^{2D}\left(\widehat{W}_t\right)\right)$ and $\delta\left(\Psi^{2D}\left(\hat{\kappa}_t\right)\right)$ was selected to be 3 and the proper value of r for $\delta\left(\Psi^{2D}\left(\hat{\kappa}_t\right)\right)$ was determined to be 2, 3, 3 and 4 for f_c = 30 kHz, 50 kHz, 70 kHz and 90 kHz, respectively, based on Eq. (23). Damage index RMS (W_t), $\delta\left(\widehat{W}_t\right)$, $\delta\left(\Psi^{2D}\left(\widehat{W}_t\right)\right)$ and $\delta\left(\Psi^{2D}\left(\hat{\kappa}_t\right)\right)$ of waveforms associated with f_c = 30 kHz were calculated and shown in Figs. 8 (a) through (d), respectively. In Fig. 8(a), large index values are observed within and beyond the damage area, and those in the latter lead to false positive identification results of the location and extent of the damage. A similar observation can be made to $\delta\left(\widehat{W}_t\right)$ in Fig. 8(b). Hence it was hard to identify the damage location and extent based on RMS (W_t) and $\delta\left(\widehat{W}_t\right)$. In Fig. 8(c), large index values can be observed within the neighborhood of the damage area, while relatively large index values can still be observed beyond the damage area. These observations are similar to those in the specimen #1. In Fig. 8(d), $\delta\left(\Psi^{2D}\left(\hat{\kappa}_t\right)\right)$ had the best identification result: large index values can only be observed within the neighborhoods of the damage area. Therefore, 2D-CWT with the second-order Laplacian of Gaussian function can well suppress global trends of $\widehat{W}_t$. Energy ratios χ associated with RMS (W_t), $\delta\left(\widehat{W}_t\right)$, $\delta\left(\Psi^{2D}\left(\widehat{W}_t\right)\right)$ and $\delta\left(\Psi^{2D}\left(\hat{\kappa}_t\right)\right)$ are listed in Table 1. It can be seen that damage identification results obtained from $\delta\left(\Psi^{2D}\left(\hat{\kappa}_t\right)\right)$ were better than those from RMS (W_t), $\delta\left(\widehat{W}_t\right)$ and $\delta\left(\Psi^{2D}\left(\widehat{W}_t\right)\right)$. Damage identification results

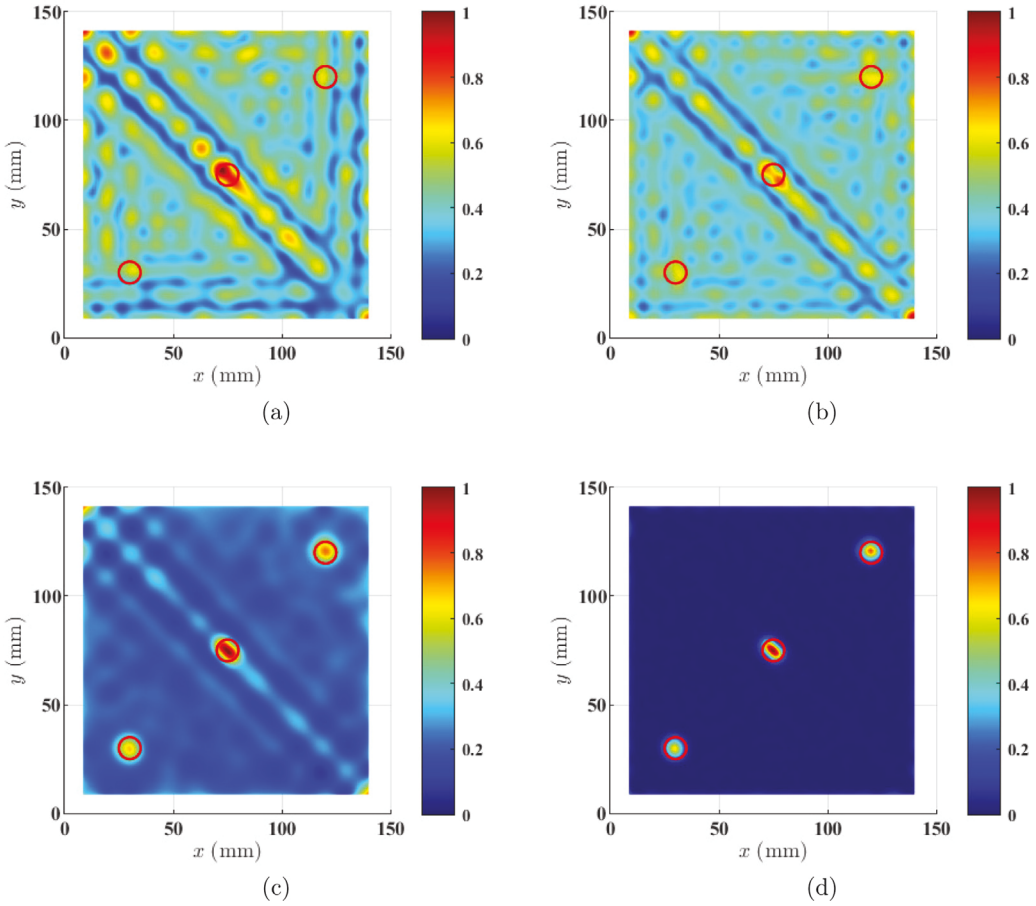

Fig. 12. Damage identification for the specimen #4 excited by the excitation with $f_c = 50$ kHz based on (a) RMS (W_t), (b) $\delta\left(\widehat{W}_t\right)$, (c) $\delta\left(\Psi^{2D}\left(\widehat{W}_t\right)\right)$, and (d) $\delta\left(\Psi^{2D}\left(\hat{\kappa}_t\right)\right)$. Locations and extent of circular damage areas are depicted by solid red lines. For better comparison, the damage values shown in each figure are normalized so that their maximum value is equal to one.

Table 1
Energy ratios χ associated with RMS (W_t), $\delta\left(\widehat{W}_t\right)$, $\delta\left(\Psi^{2D}\left(\widehat{W}_t\right)\right)$ and $\delta\left(\Psi^{2D}\left(\hat{\kappa}_t\right)\right)$ in the specimen #3 at different values of f_c (unit: %).

f_c	RMS (W_t)	$\delta\left(\widehat{W}_t\right)$	$\delta\left(\Psi^{2D}\left(\widehat{W}_t\right)\right)$	$\delta\left(\Psi^{2D}\left(\hat{\kappa}_t\right)\right)$
30 kHz	5.3	6.5	10.0	16.2
50 kHz	5.3	5.4	6.9	12.1
70 kHz	5.0	5.3	6.3	14.6
90 kHz	5.3	5.0	5.7	14.5

using the waveforms associated with the f_c = 50 kHz, 70 kHz and 90 kHz are shown in Figs. 9 through 11, respectively, and corresponding χ are listed in Table 1. It can be seen that the damage location and extent cannot be identified based on RMS (W_t), $\delta\left(\widehat{W}_t\right)$ and $\delta\left(\Psi^{2D}\left(\widehat{W}_t\right)\right)$, while $\delta\left(\Psi^{2D}\left(\hat{\kappa}_t\right)\right)$ can consistently identify the location and extent of the damage accurately.

4.3. Experimental test and damage identification for specimen #4

The specimen #4 was studied to validate the effectiveness of the proposed damage identification method for multiple damage areas with relatively small sizes than that in the specimen #3. The specimen #4 had a length of 150 mm, a width of 150 mm, and a thickness of 3 mm. Three circular damage in the form of 50% thickness reduction with a diameter of 10 mm were introduced to the specimen; they were centered at $(30, 30)$ mm, $(75, 75)$ mm and $(120, 120)$ mm. Dimensions and locations of the damage areas can be found in Fig. 5(c). A PZT actuator with a diameter of 7 mm was attached to the upper left corner of the specimen #4 to generate five-count wave packets with two f_c, including 50 kHz and 75 kHz, for generating excitation forces. The same instruments as those for the specimen #3 were used. The peak-to-peak amplitude of the excitation forces were amplified to 150 V. A grid of

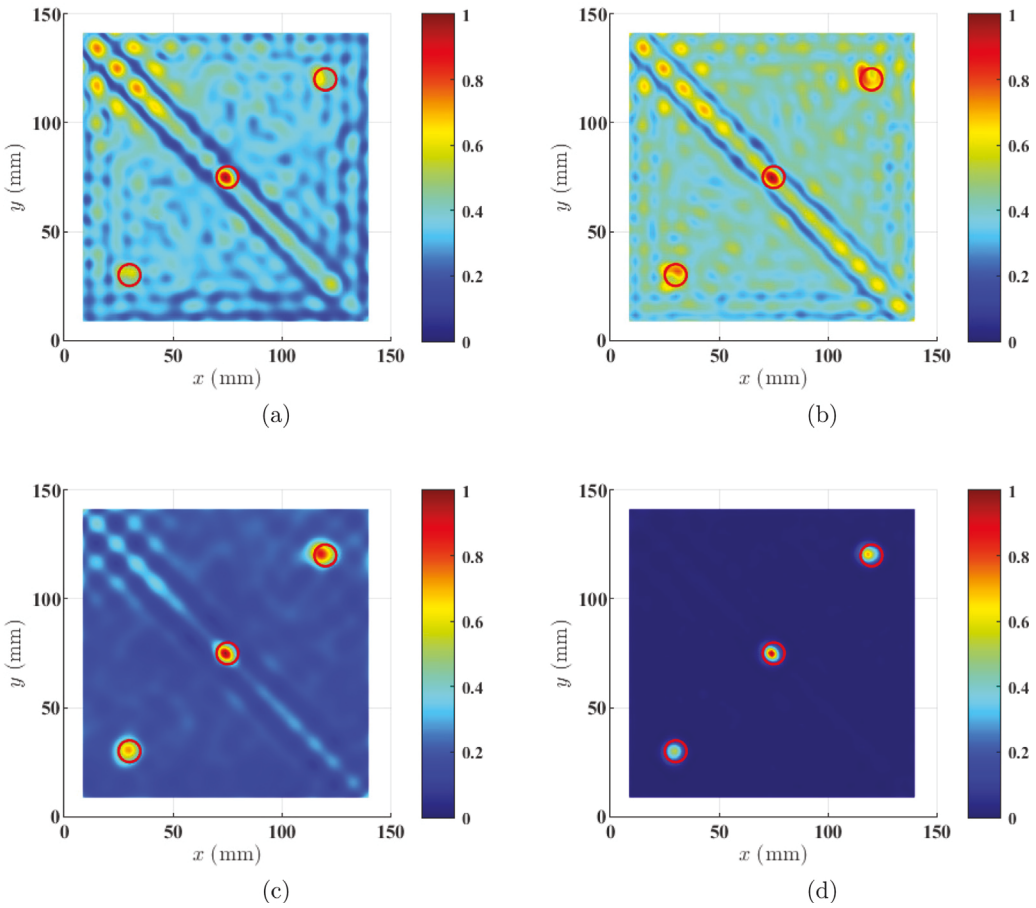

Fig. 13. Damage identification for the specimen #4 excited by the excitation with $f_c = 75$ kHz based on (a) RMS (W_t), (b) $\delta\left(\widehat{W}_t\right)$, (c) $\delta\left(\Psi^{2D}\left(\widehat{W}_t\right)\right)$, and (d) $\delta\left(\Psi^{2D}\left(\hat{\kappa}_t\right)\right)$. Locations and extent of circular damage areas are depicted by solid red lines. For better comparison, the damage values shown in each figure are normalized so that their maximum value is equal to one.

103 × 103 measurement points was assigned to the whole intact side of the specimen #4. A sampling frequency of 1.25 MHz was used to measure the response of each measurement point for 10 ms. For each measured response, 50 averages were carried out to minimize adverse effects of measurement errors. The averaged measured responses of all measurement points were reconstructed as 2D waveforms at each measurement instant. It was taken about three hours to finish the whole measurement process in each case of excitation force. Phase velocity dispersion curves for the specimen #4 are same to those of the specimen #3 as they were made of the same material. Based on the phase velocity dispersion curves, only the S0 and A0 Lamb wave modes existed for all f_c.

The value of s for $\delta\left(\widehat{W}_t\right)$, $\delta\left(\Psi^{2D}\left(\widehat{W}_t\right)\right)$ and $\delta\left(\Psi^{2D}\left(\hat{\kappa}_t\right)\right)$ was selected to be 3 and the proper value of r for $\delta\left(\Psi^{2D}\left(\hat{\kappa}_t\right)\right)$ was determined to be 2 for the two excitation cases based on Eq. (23). Damage indexes RMS (W_t), $\delta\left(\widehat{W}_t\right)$, $\delta\left(\Psi^{2D}\left(\widehat{W}_t\right)\right)$ and $\delta\left(\Psi^{2D}\left(\hat{\kappa}_t\right)\right)$ associated with the excitation with $f_c = 50$ kHz are shown in Fig. 12. In Fig. 12(a), large index values are observed within and beyond the three damage areas. A similar observation can be made to $\delta\left(\widehat{W}_t\right)$ in Fig. 12(b). Hence it was hard to identify the damage locations and extent based on RMS (W_t) and $\delta\left(\widehat{W}_t\right)$. In Fig. 12(c), large index values can be observed within the neighborhoods of the three damage areas, while relatively large index values can still be observed beyond these damage areas. It is because TEO can only partially suppress global trends of $\widehat{W}_t$. In Fig. 12(d), $\delta\left(\Psi^{2D}\left(\hat{\kappa}_t\right)\right)$ had the best identification result. In addition, 2D-CWT with the second-order Laplacian of Gaussian function can well suppress global trends of $\widehat{W}_t$. Energy ratios χ associated with RMS (W_t), $\delta\left(\widehat{W}_t\right)$, $\delta\left(\Psi^{2D}\left(\widehat{W}_t\right)\right)$ and $\delta\left(\Psi^{2D}\left(\hat{\kappa}_t\right)\right)$ are listed in Table 2. It can be seen that damage identification results obtained from $\delta\left(\Psi^{2D}\left(\hat{\kappa}_t\right)\right)$ were the best. Damage indexes and χ associated with the excitation with $f_c = 75$ kHz are shown in Fig. 13 and listed in Table 2, respectively to further verify the effectiveness of the proposed damage identification method.

Table 2
Energy ratios χ associated with RMS (W_t), $\delta\left(\widehat{W}_t\right)$, $\delta\left(\Psi^{2D}\left(\widehat{W}_t\right)\right)$ and $\delta\left(\Psi^{2D}\left(\widehat{\kappa}_t\right)\right)$ in the specimen #4 at different values of f_c (unit: %).

f_c	RMS (W_t)	$\delta\left(\widehat{W}_t\right)$	$\delta\left(\Psi^{2D}\left(\widehat{W}_t\right)\right)$	$\delta\left(\Psi^{2D}\left(\widehat{\kappa}_t\right)\right)$
50 kHz	4.2	4.2	12.7	88.5
75 kHz	4.7	4.8	13.8	93.5

5. Concluding remarks

In this paper, a baseline-free damage identification method is proposed for plate-like structures by extracting damage-induced local anomalies in 2D-CPFWs. The fundamental mechanism of suppressing the global trends of 2D-CPFW by 2D-CWT is investigated. It is found that the rth-order Laplacian of Gaussian function can well suppress the global trend of a 2D-CPFW within a finite interval if the trend can be well approximated by a $(2r-1)$th-order bi-variant polynomial. The effectiveness of the proposed method is numerically and experimentally investigated with different numbers, extent and locations of damage areas and central frequencies of excitation forces. It was found that (1) the proper order of the Laplacian of Gaussian function can be determined based on the modal assurance criterion and statistical criterion, (2) the proposed method is robust against measurement noise and effective for different damage scenarios and central frequencies of excitation forces, and (3) the proposed method can accurately identify the location and extent of damage when local anomalies cause are not noticeably in PFWs. The total duration of a measurement process increases with the density of measurement points, the number of averages and the duration of each average for a measurement point. One future investigation can focus on the effects of decreases of the density of measurement points, the number and duration of averages on damage identification results by the proposed method. Another two future investigations can focus on determining the proper value of the scale parameter in the CWT for the proposed method and its applications to complex engineering structures, such as composite plates.

CRediT authorship contribution statement

Wei Zhou: Methodology, Software, Experimental test data acquiring, Writing – original draft. **Y.F. Xu:** Supervision, Conceptualization, Methodology, Writing – review & editing, Funding acquisition. **J.S. Kim:** Experimental test data acquiring.

Declaration of competing interest

The authors declare that they have no known competing financial interests or personal relationships that could have appeared to influence the work reported in this paper.

Acknowledgments

The authors are grateful for the financial support from the National Science Foundation, USA through Grant No. CMMI-1762917. The authors are also grateful for the anonymous reviewers for their constructive comments and suggestions.

Appendix. 2D-CWT

A mother wavelet function $\psi(x,y)$ has a zero mean [31]:

$$\int_{-\infty}^{\infty}\int_{-\infty}^{\infty}\psi(x,y)\,\mathrm{d}x\mathrm{d}y=0 \tag{A.1}$$

Further, if $\psi(x,y)$ is rotation-invariant, there are a family of associated mother wavelet functions, which can be expressed by

$$\psi_{u,v,s}(x,y)=\frac{1}{s}\psi\left(\frac{x-u}{s},\frac{y-v}{s}\right) \tag{A.2}$$

where s is the scale parameter, and u and v are translation parameters along x- and y-axes, respectively. Let $f(x,y)\in L^2\left(\mathbb{R}^2\right)$, 2D-CWT of $f(x,y)$ with $\psi(x,y)$ is defined as

$$\widehat{f}(u,v,s)=\frac{1}{s}\int_{-\infty}^{\infty}\int_{-\infty}^{\infty}f(x,y)\,\overline{\psi}\left(\frac{x-u}{s},\frac{y-v}{s}\right)\mathrm{d}x\mathrm{d}y=\left(\tilde{\psi}_s\otimes f\right)(u,v) \tag{A.3}$$

where

$$\tilde{\psi}_s(x,y)=\frac{1}{s}\overline{\psi}\left(\frac{-x}{s},\frac{-y}{s}\right) \tag{A.4}$$

and $\overline{(\cdot)}$ is the complex conjugate of a function. The mother wavelet $\psi(x,y)$ has N vanishing moments if

$$\int_{-\infty}^{\infty}\int_{-\infty}^{\infty}x^{\beta}y^{\alpha-\beta}\psi(x,y)\,\mathrm{d}x\mathrm{d}y=0,\quad 0\leqslant\alpha<N \tag{A.5}$$

where α and β are both non-negative integers with $\beta\leqslant\alpha$.

References

[1] Y. Bao, Y. Guo, H. Li, A machine learning–based approach for adaptive sparse time–frequency analysis used in structural health monitoring, Struct. Health Monit. 19 (6) (2020) 1963–1975.
[2] C.B. Smith, E.M. Hernandez, Non-negative and sparsity constrained inverse problems in damage identification–application to a full-scale 3D truss, Mech. Syst. Signal Process. 140 (2020) 106648.
[3] Y. Song, Z. Liu, A. Rønnquist, P. Nåvik, Z. Liu, Contact wire irregularity stochastics and effect on high-speed railway pantograph–catenary interactions, IEEE Trans. Instrum. Meas. 69 (10) (2020) 8196–8206.
[4] W. Fan, P. Qiao, Vibration-based damage identification methods: A review and comparative study, Struct. Health Monit. 10 (1) (2011) 83–111.
[5] K.H. Padil, N. Bakhary, M. Abdulkareem, J. Li, H. Hao, Non-probabilistic method to consider uncertainties in frequency response function for vibration-based damage detection using artificial neural network, J. Sound Vib. 467 (2020) 115069.
[6] M.-S. Huang, M. Gül, H.-P. Zhu, Vibration-based structural damage identification under varying temperature effects, J. Aerosp. Eng. 31 (3) (2018) 04018014.
[7] O. Avci, O. Abdeljaber, S. Kiranyaz, M. Hussein, M. Gabbouj, D.J. Inman, A review of vibration-based damage detection in civil structures: From traditional methods to machine learning and deep learning applications, Mech. Syst. Signal Process. 147 (2021) 107077.
[8] Y. Xu, J. Kim, Baseline-free structural damage identification for beam-like structures using curvature waveforms of propagating flexural waves, Sensors 21 (7) (2021) 2453.
[9] R. Adams, D. Walton, J. Flitcroft, D. Short, Vibration testing as a nondestructive test tool for composite materials, in: Composite Reliability, ASTM International, 1975.
[10] R. Adams, P. Cawley, C. Pye, B. Stone, A vibration technique for non-destructively assessing the integrity of structures, J. Mech. Eng. Sci. 20 (2) (1978) 93–100.
[11] H. Hu, B.-T. Wang, C.-H. Lee, J.-S. Su, Damage detection of surface cracks in composite laminates using modal analysis and strain energy method, Compos. Struct. 74 (4) (2006) 399–405.
[12] A. Pandey, M. Biswas, M. Samman, Damage detection from changes in curvature mode shapes, J. Sound Vib. 145 (2) (1991) 321–332.
[13] C.P. Ratcliffe, A frequency and curvature based experimental method for locating damage in structures, ASME J. Vib. Acoust. 122 (3) (2000) 324–329.
[14] M. Rucka, K. Wilde, Application of continuous wavelet transform in vibration based damage detection method for beams and plates, J. Sound Vib. 297 (3–5) (2006) 536–550.
[15] W. Xu, M. Radzieński, W. Ostachowicz, M. Cao, Damage detection in plates using two-dimensional directional Gaussian wavelets and laser scanned operating deflection shapes, Struct. Health Monit. 12 (5–6) (2013) 457–468.
[16] M. Cao, W. Xu, W. Ostachowicz, Z. Su, Damage identification for beams in noisy conditions based on Teager energy operator-wavelet transform modal curvature, J. Sound Vib. 333 (6) (2014) 1543–1553.
[17] W. Xu, K. Ding, J. Liu, M. Cao, M. Radzieński, W. Ostachowicz, Non-uniform crack identification in plate-like structures using wavelet 2D modal curvature under noisy conditions, Mech. Syst. Signal Process. 126 (2019) 469–489.
[18] M. Cao, M. Radzieński, W. Xu, W. Ostachowicz, Identification of multiple damage in beams based on robust curvature mode shapes, Mech. Syst. Signal Process. 46 (2) (2014) 468–480.
[19] W. Xu, M. Cao, W. Ostachowicz, M. Radzieński, N. Xia, Two-dimensional curvature mode shape method based on wavelets and Teager energy for damage detection in plates, J. Sound Vib. 347 (2015) 266–278.
[20] H. Lamb, On waves in an elastic plate, Proc. Royal Soc. London. Ser. A 93 (648) (1917) 114–128.
[21] W. Staszewski, B. Lee, L. Mallet, F. Scarpa, Structural health monitoring using scanning laser vibrometry: I. Lamb wave sensing, Smart Mater. Struct. 13 (2) (2004) 251–260.
[22] L. Mallet, B. Lee, W. Staszewski, F. Scarpa, Structural health monitoring using scanning laser vibrometry: II. Lamb waves for damage detection, Smart Mater. Struct. 13 (2) (2004) 261–269.
[23] M. Ruzzene, S. Jeong, T. Michaels, J. Michaels, B. Mi, Simulation and measurement of ultrasonic waves in elastic plates using laser vibrometry, in: AIP Conference Proceedings, Vol. 760, no. 1, American Institute of Physics, 2005, pp. 172–179.
[24] A. Żak, M. Radzieński, M. Krawczuk, W. Ostachowicz, Damage detection strategies based on propagation of guided elastic waves, Smart Mater. Struct. 21 (3) (2012) 035024.
[25] M. Ruzzene, Frequency–wavenumber domain filtering for improved damage visualization, Smart Mater. Struct. 16 (6) (2007) 2116–2129.
[26] L. Yu, Z. Tian, Lamb wave structural health monitoring using a hybrid PZT-laser vibrometer approach, Struct. Health Monit. 12 (5–6) (2013) 469–483.
[27] G. Sha, H. Xu, M. Radzieński, M. Cao, W. Ostachowicz, Z. Su, Guided wavefield curvature imaging of invisible damage in composite structures, Mech. Syst. Signal Process. 150 (2021) 107240.
[28] V. Giurgiutiu, Structural Health Monitoring: With Piezoelectric Wafer Active Sensors, Elsevier, 2007.
[29] G.B. Santoni, L. Yu, B. Xu, V. Giurgiutiu, Lamb wave-mode tuning of piezoelectric wafer active sensors for structural health monitoring, J. Vib. Acoust. 129 (6) (2007) 752–762.
[30] M. Yoon, D. Heider, J. Gillespie Jr., C. Ratcliffe, R. Crane, Local damage detection using the two-dimensional gapped smoothing method, J. Sound Vib. 279 (1–2) (2005) 119–139.
[31] J.-P. Antoine, R. Murenzi, P. Vandergheynst, S.T. Ali, Two-Dimensional Wavelets and Their Relatives, Cambridge University Press, 2008.
[32] S. Mallat, A Wavelet Tour of Signal Processing, Elsevier, 1999.
[33] Y. Xu, W. Zhu, J. Liu, Y. Shao, Identification of embedded horizontal cracks in beams using measured mode shapes, J. Sound Vib. 333 (23) (2014) 6273–6294.
[34] Y. Xu, W. Zhu, Non-model-based damage identification of plates using measured mode shapes, Struct. Health Monit. 16 (1) (2017) 3–23.
[35] M. Solís, M. Algaba, P. Galvín, Continuous wavelet analysis of mode shapes differences for damage detection, Mech. Syst. Signal Process. 40 (2) (2013) 645–666.
[36] R. Kumar, R. Nigam, S.K. Singh, Selection of suitable mother wavelet along with vanishing moment for the effective detection of crack in a beam, Mech. Syst. Signal Process. 163 (2022) 108136.
[37] W. Xu, W. Zhu, Y. Xu, M. Cao, A comparative study on structural damage detection using derivatives of laser-measured flexural and longitudinal vibration shapes, J. Nondestruct. Eval. 39 (3) (2020) 1–17.
[38] M.R. Taha, A. Noureldin, J. Lucero, T. Baca, Wavelet transform for structural health monitoring: A compendium of uses and features, Struct. Health Monit. 5 (3) (2006) 267–295.
[39] R.J. Allemang, The modal assurance criterion–twenty years of use and abuse, Sound Vib. 37 (8) (2003) 14–23.
[40] R.E. Walpole, Probability & Statistics for Engineers & Scientists, Prentice Hall, 2006.
[41] J.F. Kaiser, On a simple algorithm to calculate the 'energy' of a signal, in: International Conference on Acoustics, Speech, and Signal Processing, IEEE, 1990, pp. 381–384.
[42] A.-O. Boudraa, E.-H.S. Diop, Image contrast enhancement based on 2D Teager-Kaiser operator, in: 2008 15th IEEE International Conference on Image Processing, IEEE, 2008, pp. 3180–3183.